Korean J. Chem. Eng., 38(7), 1358-1369 (2021)
DOI: 10.1007/s11814-021-0817-1

pISSN: 0256-1115
eISSN: 1975-7220

Computational fluid dynamic analysis of mass transfer and hydrodynamics in a planetary centrifugal bioreactor

Baojun Shen*,, Xiaobin Zhan*,**, Yu He*,**, Zhibin Sun*,**, Jiecai Long*,**, Yili Yang*,**, and Xiwen Li*,**,†**

*State Key Laboratory of Digital Manufacturing Equipment and Technology, Huazhong University of Science and Technology, Wuhan 430074, China
**School of Mechanical Science and Engineering, Huazhong University of Science and Technology, Wuhan 430074, China
(*Received 4 January 2021 • Revised 30 March 2021 • Accepted 23 April 2021*)

Abstract−Planetary centrifugal bioreactors are promising candidates for cell culture platforms since there is no pollution caused by stirring blades. In this work, the fluid structure in a planetary centrifugal bioreactor was investigated using the computational fluid dynamics (CFD) method. The effects of operating conditions on the oxygen transfer rate (OTR), mixing efficiency and shear environment of the bioreactor were studied with the revolution speed (N) ranging from 60 to 160 rpm and the rotation-to-revolution speed ratio (i) from −2 to 1. The results show that the volumetric mass transfer coefficient (k_La), turbulence intensity, volumetric power consumption, and shear stress increase along with the increase of the revolution and rotation speeds. Furthermore, the rotation in the opposite direction to the revolution is beneficial to the performance of the bioreactor. The planetary centrifugal bioreactor has a higher k_La of 50-200/h and a lower average shear stress of 0.01-0.05 Pa in comparison with conventional stirred tank bioreactors, which makes it suitable for biological culture of oxygen-consuming cells and shear-sensitive cells.

Keywords: Planetary Centrifugal Bioreactor, CFD, Oxygen Transfer, Mixing, Shear Stress

INTRODUCTION

Bioreactors are playing a more and more important role in medicine, food, cosmetics and other industries [1-3]. In the past few decades, bioreactors have been often used for cell culture to obtain a wide variety of recombinant proteins, antibiotics, vaccines, enzymes, antibodies and so on [4,5], which become an indispensable part in the production of biological products. However, the activity and metabolic yields of cells in culture mediums are affected by the mixing capacity, shear stress level, interphase mass transfer rate, turbulence intensity and other parameters of bioreactors [6-8].

One of the most conventional bioreactors is the stirred tank bioreactor, whose mixing and mass transfer process have been intensively studied [9-11]. According to Buffo et al. [1], the stirred tank bioreactor has both axial and radial mixing characteristics, so the homogenization of flow field and component concentration can be realized rapidly. However, to improve the oxygen transfer rate (OTR), strong agitation is usually needed in stirred tank bioreactors to intensify the turbulence effects of fluids [12,13], which leads to a large shear stress near impellers [14]. For some shear-sensitive cells, e.g., mammalian cells, a large shear stress will reduce their activity and even cause irreversible damage to them [15-17]. As a result, the quality and yield of cell culture are limited in stirred tank bioreactors.

A new type of blade-free bioreactor is expected to make up for the deficiency of stirred tank bioreactors, that is, the planetary centrifugal bioreactor. The vessel of the planetary centrifugal bioreactor is tilted for a certain angle onto the horizontal plane, which rotates around its own geometric axis while revolving around the central axis of the bioreactor. The centrifugal forces generated by rotation and revolution interact with each other to push the materials inside the vessel to flow, thus achieving efficient and uniform mixing [18]. This technology has been successfully applied to the preparation of colloids, pastes, resins and creams [19-21]. Compared to other bioreactors equipped with stirring blades, the planetary centrifugal bioreactor causes less damage and pollution to materials [22,23]. Hence, the planetary centrifugal bioreactor has a great potential for culturing shear-sensitive cells.

To the best of the authors' knowledge, there is no published research discussing the application of planetary centrifugal bioreactors in cell culture so far. However, the orbitally shaken bioreactor, which works in a similar way to the planetary centrifugal bioreactor, has found wide applications in cell culture [24-27]. The vessel of the orbitally shaken bioreactor remains vertical, whose rotation and revolution speeds are equal but in the opposite directions [28]. Liu et al. [29] studied the distribution of shear stress in an orbitally shaken bioreactor with the revolution speed in the range of 115-220 rpm, and analyzed the influence of shear stress on the cell activity. Zhu et al. [30] simulated the volumetric mass transfer coefficient (k_La) in an orbitally shaken bioreactor at different speeds and filling volumes, and found that k_La was sufficient to meet the oxygen demand of high-density cell culture. The rotation-to-revolution speed ratio of the orbitally shaken bioreactor is −1, so it is a special planetary centrifugal bioreactor. Thus, it could be speculated that the planetary centrifugal bioreactor which is distinguished by a flexible rotation-to-revolution speed ratio has a broader applica-

†To whom correspondence should be addressed.
E-mail: xiwenli@hust.edu.cn

tion prospect in cell culture.

The purpose of this study is to explore the potential of planetary centrifugal bioreactors as an alternative technique for cell culture. First, the computational fluid dynamics (CFD) method was validated by comparing the simulated gas-liquid interface shapes and liquid levels in the planetary centrifugal bioreactor with the experimental data. Then, the specific mass transfer area and turbulence dissipation rate obtained by simulations were used to estimate k_La. Finally, the fluid velocity field, the turbulence intensity and the volumetric power consumption were simulated at different revolution and rotation speeds, and the influences of operating conditions on the mixing performance of the planetary centrifugal bioreactor were investigated. The distribution of shear stress in the planetary centrifugal bioreactor was numerically computed under different operating conditions and the results were compared with those of conventional stirred tank bioreactors.

NUMERICAL METHODS

1. Physical Model

The planetary centrifugal bioreactor studied in this paper is equipped with a cylindrical vessel made of transparent glass with a radius of r=31 mm and a height of H=75 mm, which is tilted for a certain angle α onto the horizontal plane, rotates around its geometric axis at an angular velocity ω while revolving around the central axis (*Z*-axis) of the bioreactor at an angular velocity Ω, as shown in Fig. 1.

The bottom center P of the vessel is initially located on the positive *X*-axis. After a period of time t (s), the vessel gyrates for a certain angle β in a counterclockwise direction. The angular velocity components generated by the rotation and revolution of the vessel are calculated as follows:

$$\begin{cases} \omega_x = -\pi i N \cos\alpha \cos\beta/30 \\ \omega_y = -\pi i N \cos\alpha \sin\beta/30 \\ \omega_z = (1+i\sin\alpha)\pi N/30 \end{cases} \quad (1)$$

where N is the revolution speed (rpm) and i represents the rotation-to-revolution speed ratio. When i>0, the rotation is in the same direction as the revolution; when i=0, the vessel does not rotate around its own geometric axis but around the central axis of the bioreactor only; when i<0, the direction of rotation is opposite to that of revolution.

The bottom center P of the vessel moves on the XOY plane, so its velocity components are described as follows:

$$\begin{cases} v_x = -\pi N R \sin\beta/30 \\ v_y = \pi N R \cos\beta/30 \\ v_z = 0 \end{cases} \quad (2)$$

where R is the radius of revolution. Since the vessel is tilted, a part of the vessel is below the XOY plane.

2. Grid Generation

Since the planetary centrifugal bioreactor involves movement and rotation in space when it works, it is difficult to characterize the spatial flow of materials with a two-dimensional model. Therefore, in this paper, a three-dimensional model was used to carry out simulations. The cylindrical simulation domain is divided into structured hexahedral grids using the commercial software ANSYS ICEM CFD (ANSYS Inc., USA), as shown in Fig. 2. Compared with unstructured grids, structured grids have the advantage of less numerical diffusion and more accurate results [31]. Moreover, structured grids provide a high solution stability and a fast convergence rate, as reported by Bumrungthaichaichan [32].

The entire computational domain consists of two parts: vessel zone and lid zone. The two zones are connected with each other through the mesh interface. The fluid flows in the vessel zone, and the purpose of the lid zone is to provide a reference zone for the rotational movement of the vessel zone. The specific rotation and revolution modeling strategies are discussed in detail in the next section.

3. Boundary Conditions

The sliding mesh (SM) approach is reported to be more accurate than the multiple reference frame (MRF) in predicting the turbulence of the flow in spite of the higher computational cost [33]. In the present study, the SM method is employed to simulate the

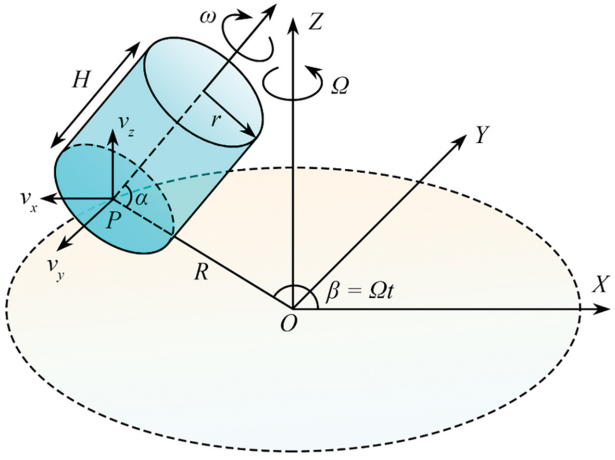

Fig. 1. Geometric model of spatial motion of the planetary centrifugal bioreactor.

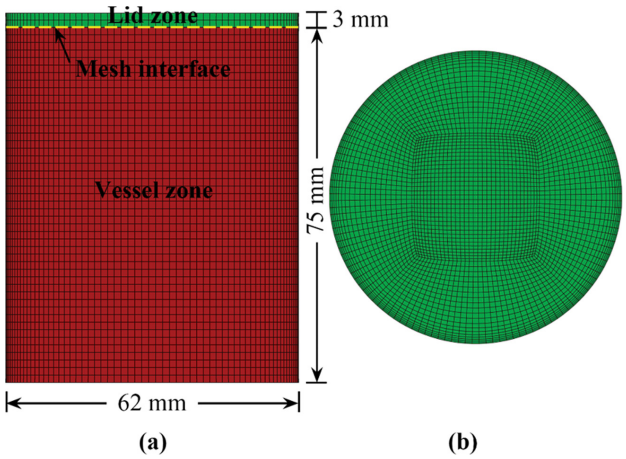

Fig. 2. Grid generation of cylindrical computational domain. (a) Front view. (b) Top view.

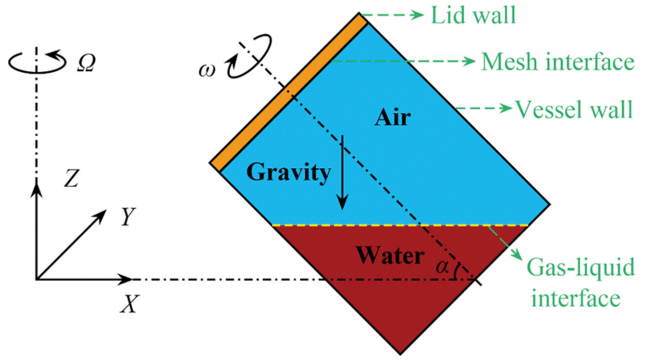

Fig. 3. Boundary conditions of the planetary centrifugal bioreactor.

rotation and revolution of the vessel. The lid zone (marked in yellow) revolves around the *Z*-axis at an angular velocity Ω while the vessel zone (marked in blue and red) rotates around its own axis at an angular velocity ω relative to the lid zone, as shown in Fig. 3. In this way, the modeling of rotation and revolution of the vessel is accomplished in the absolute coordinate system. Note that the lid zone is an imaginary auxiliary zone, and its motion pattern has no actual representative significance.

The lower part of the vessel zone is filled with 20 mL water marked in red, and the upper part of the vessel zone is filled with air marked in blue. The gas-liquid interface is defined as a deformable free surface. Under the action of gravity, the gas-liquid interface is horizontal at the initial time. To avoid the flow of fluids from the vessel zone into the lid zone, the lid zone is set as a solid zone. The vessel wall is set as a moving wall, and its rotational speed is set to zero relative to the motion of the vessel zone. It is assumed that the vessel wall is adiabatic and no heat exchange occurs between the vessel wall and the culture medium. In addition, the no-slip boundary condition is applied to the vessel wall, and the scalable wall functions are adopted to deal with the near-wall regions.

4. Two-phase Flow Model

The planetary centrifugal bioreactor contains the gas-liquid two-phase fluids which are initially separated from each other and the interface is very clear. The volume of fluid (VOF) model under Euler grid is suitable for this two-phase flow system, and has been demonstrated to be a reliable method for studying the fluid flow in a bioreactor [29]. In this paper, the VOF model is used to track the position and shape of the gas-liquid interface. The volume fraction of the gas phase can be determined by

$$\frac{\partial \gamma}{\partial t}+\mathbf{U}_G\cdot\nabla\gamma=0 \tag{3}$$

where $\mathbf{U}_G$ is the velocity vector of the gas phase, γ is the volume fraction of the gas phase, thus the volume fraction of the liquid phase can be calculated as $1-\gamma$. When γ=0, the calculation domain contains the liquid phase only; when γ=1, the calculation domain contains the gas phase only.

Therefore, the density and viscosity of the gas-fluid mixture are averaged with the corresponding weighting factor:

$$\rho=\gamma\rho_G+(1-\gamma)\rho_L \tag{4}$$

$$\mu=\gamma\mu_G+(1-\gamma)\mu_L \tag{5}$$

where the subscripts G and L represent the gas phase and the liquid phase, respectively.

5. Governing Equations

In general, the viscosity of cell culture mediums is similar to that of water [34]. For a given planetary system, the Reynolds number is defined as follows [35]:

$$\mathrm{Re}=\frac{\rho\times u_{ch}\times d}{\mu} \tag{6}$$

$$u_{ch}=2NR+2|i-1|Nr \tag{7}$$

where u_{ch} is the characteristic velocity of the planetary centrifugal bioreactor (m/s), the characteristic length d is the diameter of the vessel (m). For the geometric and operating parameters of the planetary centrifugal bioreactor within the range studied in this paper, u_{ch} obtains the minimum value when i=1 and N=60 rpm. Therefore, the minimum value of Re is calculated to be 9920. For the rotating flow in a cylindrical vessel, three flow patterns are identified based on the Reynolds number: laminar flow (Re<200), transitional flow (200<Re<500) and fully turbulent flow (Re>9,000) [36]. Therefore, the flow in the planetary centrifugal bioreactor studied in this paper is turbulent.

The rotation of the bioreactor will generate an interface with a large curvature and a high strain rate, so the RNG k-ε model is suitable to solve the turbulence transport equations. This model is an improvement of the standard k-ε model, which takes into account the influences of swirl on turbulence and improves the computation accuracy for swirling flows. It is assumed that the fluid medium is incompressible and isothermal, and there is no external source input. Thus, the mean velocity and turbulence are achieved by solving the Reynolds average equations for conservation of mass and momentum together with the turbulence model. The compact form of Reynolds-averaged Navier-Stokes (RANS) equations and transport equations for the RNG k-ε model can be written as [37]:

Table 1. Details of the variables for continuity equation, momentum equations, and transport equations of k and ε for the RNG k-ε model [37]

Equation	ϕ	Γ_φ	S_φ	Constants
Continuity	1	0	0	-
Momentum	U_i	μ	$-\frac{\partial p}{\partial x_i}+\frac{\partial}{\partial x_j}\left[\mu_t\frac{\partial U_i}{\partial x_j}\right]+S_{M,i}$	-
k-Transport	k	$\alpha_k(\mu+\mu_t)$	$G_k+G_b-\rho\varepsilon-Y_M+S_k$	-
ε-Transport	ε	$\alpha_\varepsilon(\mu+\mu_t)$	$C_{1\varepsilon}\frac{\varepsilon}{k}(G_k+C_{3\varepsilon}G_b)-C_{2\varepsilon}\rho\frac{\varepsilon^2}{k}-R_\varepsilon+S_\varepsilon$	$C_{1\varepsilon}$=1.42, $C_{2\varepsilon}$=1.68

Table 2. Geometric and operating parameters of the bioreactor for simulations

R (mm)	α (°)	N (rpm)	i
80	45	60, 90, 110, 140, 160	−2, −1.5, −1, −0.5, 0, 1

$$\frac{\partial(\rho\phi)}{\partial t}+\frac{\partial(\rho \mathbf{U}\phi)}{\partial x_j}=\frac{\partial}{\partial x_j}\left[\Gamma_\varphi\frac{\partial\phi}{\partial x_j}\right]+S_\varphi \quad (8)$$

where **U** is the mean velocity vector, ϕ is a universal variable, Γ_φ is the diffusivity, and S_φ is the source term. The details of the variables for continuity equation, momentum equations, and turbulence models are shown in Table 1.

6. Numerical Setup

The commercial software package ANSYS FLUENT (ANSYS Inc., USA) is used to simulate the flow field in the planetary centrifugal bioreactor. The geometric and operating parameters of the bioreactor for simulations are shown in Table 2.

The pressure-implicit with splitting of operators (PISO) method is employed to solve the coupling of pressure and velocity. The pressure staggering option (PRESTO!) and the least squares cell based are adopted for the spatial discretization scheme of pressure and gradient, respectively. The explicit geometric reconstruction scheme is adopted for the spatial discretization scheme of volume fraction. The momentum equations and transport equations of k and ε are spatially discretized by the second-order upwind scheme. The temporal discretization scheme is the first-order implicit. The time step is set to 1×10^{-4} s to ensure that the Courant-Friedrichs-Levy number is less than 1. The calculation for the simulations in each case on the server (Intel Xeon processer, 2.4 GHz, 96 GB RAM, 40 CPU cores) lasts for about 24 h to make sure the flow field reaches the quasi-steady state.

EXPERIMENTAL METHODS

The simulation model is validated on a bioreactor (SPH-300D, ShiPing Co., Ltd., Shanghai, China). A 235 mL cylindrical vessel is filled with the gas-liquid two-phase fluids at 25 °C. The gas phase is the standard air with a density of 1.225 kg/m^3 and a viscosity of 1.7894×10^{-5} Pa·s. The liquid phase is the deionized water with a density of 1,000 kg/m^3, a viscosity of 0.001 Pa·s and a surface tension of 0.07 N/m. The filling volume (V_L) of deionized water is selected as 20 mL. The geometric and operating parameters used in the experimental setup are shown in Table 3. $\omega_x=\omega_y=\omega_z=0$ can be calculated by substituting $\alpha=90°$ and i=−1 into Eq. (1), which shows that the motion of the bioreactor is the circular translation without rotation component. The gas-liquid interface of the liquid wave is captured by a high-speed camera, which is fixed on the experimental setup and moves along with the vessel. Thus, there is no relative motion between the vessel and the camera. In order to easily distinguish the gas-liquid interface in experiments, a little Rhodamine B is added to dye the deionized water red. The influence of Rhodamine B on the density and viscosity of the deionized water can be ignored. The height of the gas-liquid interface is measured by a scale on the wall of the transparent glass vessel.

Table 3. Geometric and operating parameters of the planetary centrifugal bioreactor for validation

R (mm)	α (°)	N (rpm)	i
25	90	80, 90, 100, 110, 120	−1

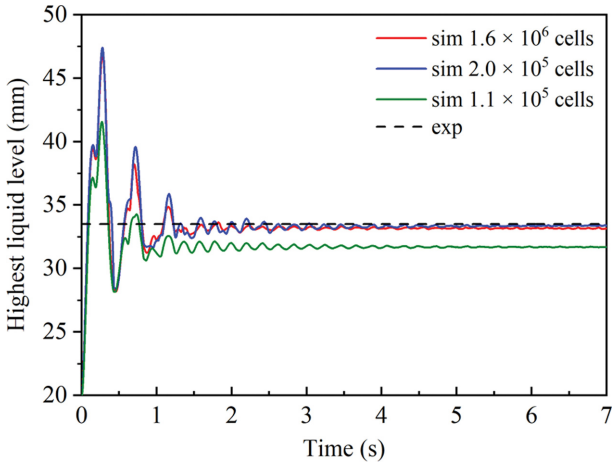

Fig. 4. Grid independence test for the CFD model at N=110 rpm and i=−1.

RESULTS AND DISCUSSION

1. Validation of the Model

To eliminate the influence of the grid number on the results of simulations, the grid independence test is carried out. Fig. 4 shows the curves of the highest liquid level as a function of time calculated by three different grid numbers as well as the experimental data obtained after the gas-liquid interface reaches a quasi-steady state. The comparison indicates that the grid number of 2.0×10^5 is enough to provide a reliable and stable solution and ensure the efficiency of simulations.

It can also be found from Fig. 4 that the gas-liquid interface fluctuates violently at first and gradually becomes stable after 2 s. This paper is focused on the performance parameters of the planetary centrifugal bioreactor after the flow field reaches the quasi-steady state. To make it easier to describe the spatial position of the vessel, a parameter β_{re} is introduced. The relationship between β_{re} and β can be expressed as $\beta_{re}=\beta-2\pi N_{re}$, where β_{re} $(0-2\pi)$ represents the phase angle of the vessel relative to the *X*-axis, and N_{re} represents the number of full revolutions. In this study, the value of N_{re} in each case is large enough to ensure that the flow field reaches the quasi-steady state.

Fig. 5 shows the qualitative comparison of the gas-liquid interface obtained from experiments and simulations after the flow field in the vessel reaches the quasi-steady state. The simulated results show that the slope angle and height of the gas-liquid interface (marked in green) both increase along with the increase of N, which is in good agreement with the experimental results, as presented in Fig. 5(a)-(e).

Interestingly, front waves of different amplitudes can be observed on the free surface under both simulation and experimental conditions as N varies from 90 to 110 rpm. At N=90 rpm, a front wave

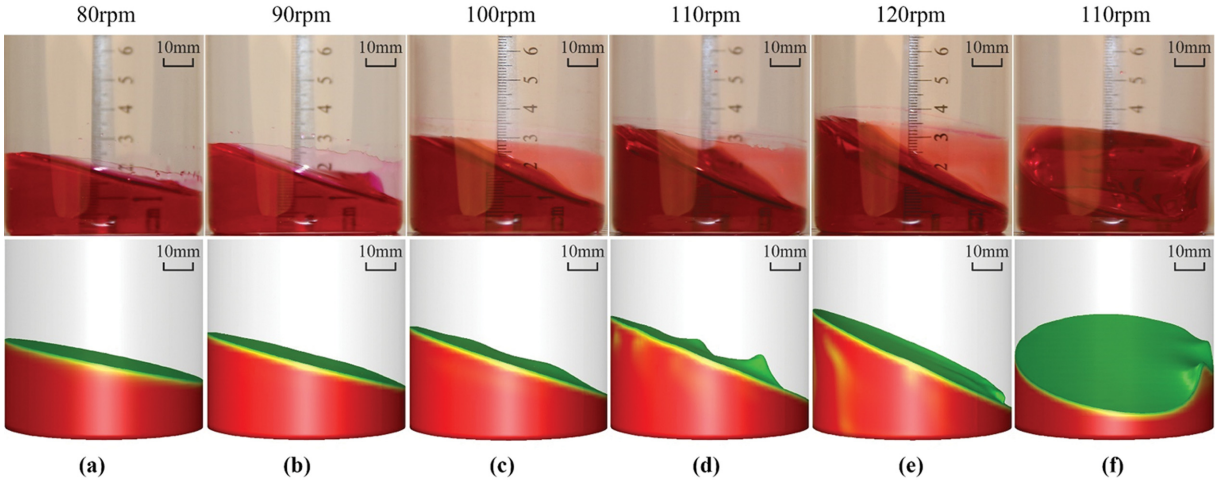

Fig. 5. Liquid wave shapes captured in experiments (upper panels) and 3D simulations (lower panels) at i=−1 and α=90°. (a)-(e) β_{re}=180° and N=80-120 rpm. (f) β_{re}=90° and N=110 rpm.

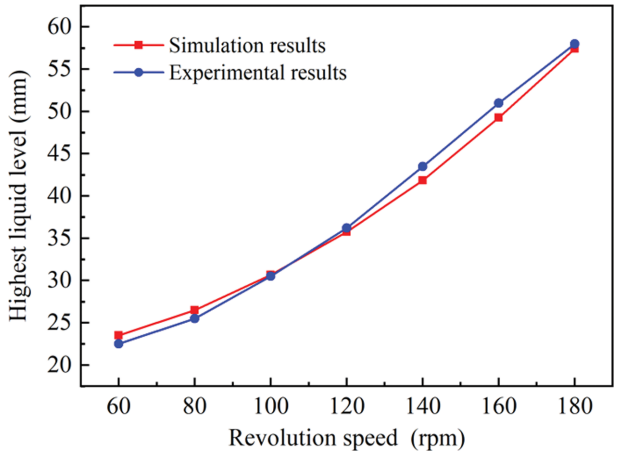

Fig. 6. Comparison of the highest liquid levels between simulated results and experimental results at different N.

begins to take shape. At N=100 rpm, two weak front waves appear under the simulation conditions, which agrees well with what is observed in experiment. At N=110 rpm, the amplitudes of the two front waves increase obviously. To better observe the two front waves from different perspectives, a view at β_{re}=90° is shown in Fig. 5(f). When N is further increased to 120 rpm, the front waves on the gas-liquid interface disappear under both experimental and simulation conditions.

For the purpose of quantitative validation, the highest liquid levels obtained by experiments and simulations at different N are plotted in Fig. 6. It can be seen that the simulated results are in good agreement with the experimental data and the maximum difference is less than 5.0%.

2. Liquid Wave Shape

Since the oxygen transfer mainly occurs at the inter-phase contact area, the shape of liquid wave is a key factor determining the oxygen transfer capacity of a bioreactor [38]. The proximal region is defined on one side of the bioreactor that is closer to the *Z*-axis, while the distal region is defined on the other side of the bioreactor, which is farther away from the *Z*-axis. Due to the effect of gravity, the liquid level is horizontal at the beginning, and the liquid is mostly concentrated in the proximal region of the bioreactor. The contours of liquid phase distribution in the bioreactor captured with different N and i at β_{re}=180° are presented in Fig. 7. It can be observed clearly that along with the increase of N, the liquid is pushed to the distal region of the bioreactor due to the action of centrifugal force. In addition, the gas-liquid interface deviates from the horizontal plane to varying degrees, forming a unimodal symmetrical wave. Therefore, the centrifugal force and gravity are the two main driving forces that change the liquid phase distribution.

As shown in Fig. 7(a), the liquid wave shapes are quite similar at N=140 rpm though i varies from 1 to −2. Thus, it can be inferred that the liquid phase distribution is not sensitive to the rotation speed. A front wave also appears at i=−2, which may be attributable to a high centrifugal force generated by a large rotation speed. Fig. 7(b) shows the effect of different N on the liquid phase distribution at i=−0.5. When N=60 rpm, the centrifugal force is small; thus, gravity plays a dominant role and the gas-liquid interface tends to remain horizontal. With the increase of N, the growing centrifugal force gradually occupies the dominant position. Therefore, the liquid is driven to the distal region of the bioreactor. Simultaneously, the angle between the gas-liquid interface and the horizontal plane shows an increasing trend.

To quantitatively describe the influence of N and i on the shape of free surface, the curves of the highest and lowest liquid levels and the mass transfer area (A) of the gas-liquid interface with respect to N and i are plotted in Fig. 8. At N=140 rpm (see Fig. 8(a)), the liquid level difference between the highest and lowest liquid levels of the gas-liquid interface slightly decreases from 58.1 mm to 50.7 mm as i increases from −2 to 1, and meanwhile A regularly decreases by 6.7%. Besides, the change rate of A with i varying from −2 to −1.5 is ten times greater than that with i varying from −1.5 to 1. This indicates that the front wave (see Fig. 7(a)) generated at i=−2 can significantly increase the interphase contact area.

Compared with the rotation-to-revolution speed ratio, the revolution speed has more notable effect on the liquid level, as can be

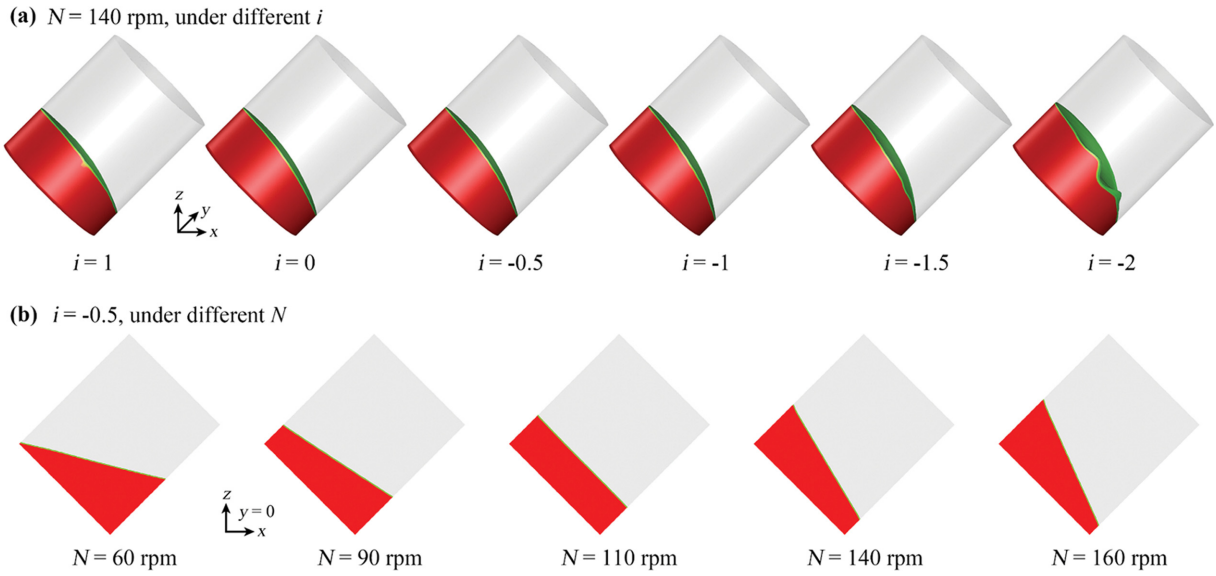

Fig. 7. Stable liquid wave shapes at β_{re}=180° under different (a) rotation-to-revolution speed ratios i and (b) revolution speeds N.

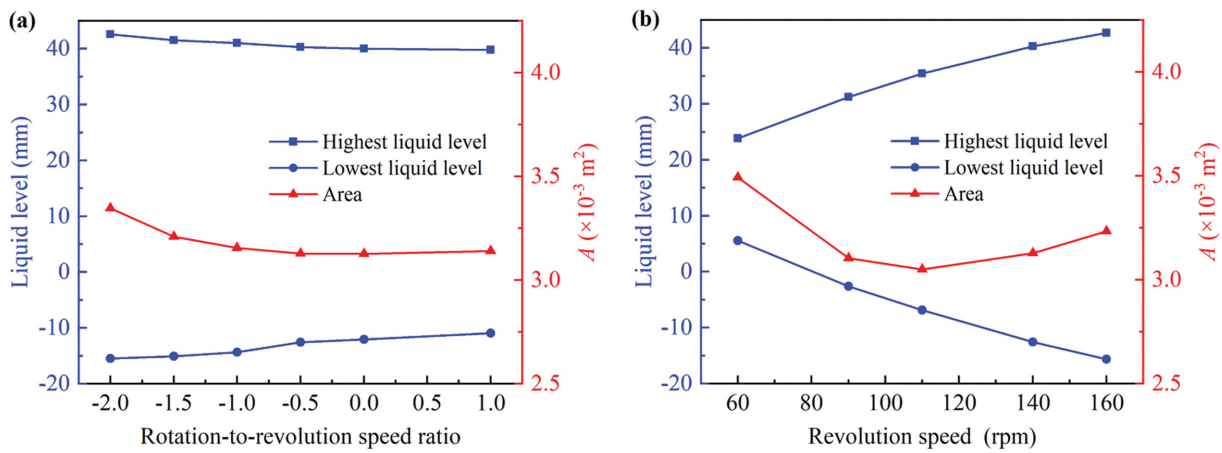

Fig. 8. Influence of revolution speed and rotation-to-revolution speed ratio on liquid level and area of gas-liquid interface. (a) N=140 rpm; (b) i=−0.5.

seen from Fig. 8(b). At i=−0.5, though the liquid level difference of the gas-liquid interface keeps expanding along with the increase of the revolution speed, the area of the gas-liquid interface does not increase linearly but decreases at first and then increases, and the minimum gas-liquid interface area is obtained at N=110 rpm. The contour of liquid phase distribution in Fig. 7(b) can account for this phenomenon. As the angle between the gas-liquid interface and the horizontal plane is expanded, the angle between the gas-liquid interface and the bottom of the bioreactor decreases at first and then increases. The gas-liquid interface is basically parallel to the bottom of the bioreactor at N=110 rpm, so the area of the gas-liquid interface is the smallest at that time.

3. Oxygen Transfer Rate

The oxygen transfer rate (OTR) between the gas phase and the liquid phase plays an important role in the growth, metabolism and protein production of cells, so it is a key parameter in the design, scale-up and operation of bioreactors [8,30]. OTR can be calculated as follows [39]:

$$OTR = k_L a(C^* - C) \tag{9}$$

where C^* represents the saturated oxygen concentration (mg/L) and C is the oxygen concentration (mg/L) in the liquid phase. OTR is in direct proportion to the volumetric mass transfer coefficient (k_La), so k_La is commonly used to evaluate the oxygen transfer capacity of bioreactors. k_La is given by [40]

$$k_L a = K \cdot \sqrt{D_L} \cdot \left(\frac{\rho\varepsilon}{\mu}\right)^{\frac{1}{4}} \cdot \frac{A}{V_L} \tag{10}$$

where K=0.4 is the model constant, D_L=1.97×10^{-9} m^2/s is the oxygen diffusion coefficient, A represents the mass transfer area, ε is the turbulence dissipation rate and V_L denotes the filling volume.

The mass transfer of oxygen mainly occurs on the gas-liquid interface, so the average turbulence dissipation rate of the gas-liq-

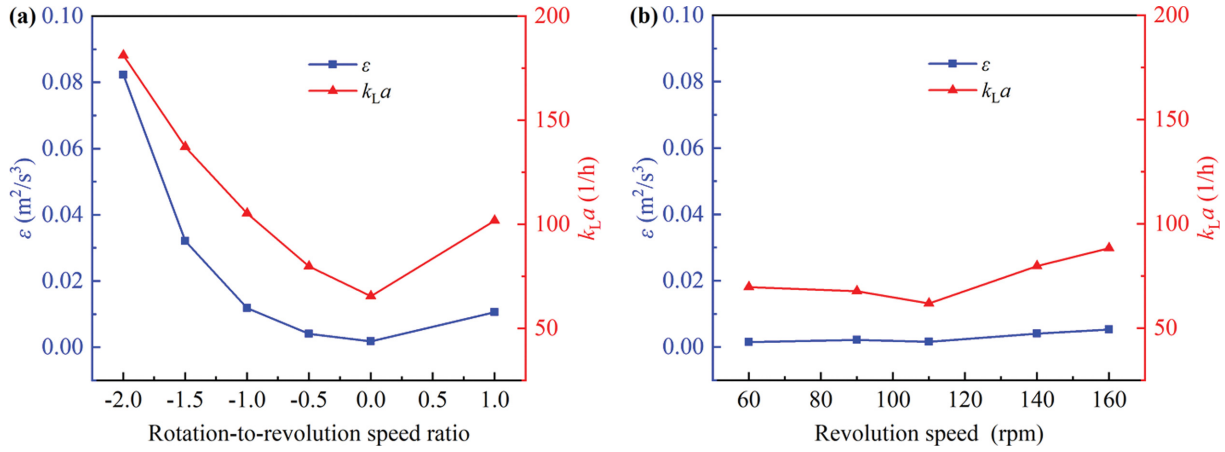

Fig. 9. Effect of revolution speed and rotation-to-revolution speed ratio on turbulence dissipation rate and volumetric mass transfer coefficient. (a) N=140 rpm; (b) i=−0.5.

uid interface is used to study the mass transfer rate [40]. Fig. 9 shows the effect of N and i on ε and k_La. It can be found that the changes of ε and k_La are comparable and follow the same trend, that is, k_La has a good dependence on ε. Furthermore, both k_La and ε are more sensitive to i than to N.

As can be seen from Fig. 9(a), k_La reaches the minimum value of 65.5/h at i=0 and the maximum value of 181.1/h at i=−2. This indicates that the rotation of the bioreactor can enhance the mass transfer rate. The main reason may be that the increasing rotation speed makes the liquid sweep a larger wall area per unit time, which increases the turbulence kinetic energy loss caused by the adhesion of the wall and the internal fluid friction. Therefore, ε rises along with the increase of the rotation speed, resulting in an increase of k_La. Note that k_La is 105.3/h at i=−1 and 101.8/h at i=1, that is, the former is 3.4% higher than the latter, suggesting that the rotation in the opposite direction to the revolution is beneficial to the improvement of k_La.

In Fig. 9(b), with i=−0.5, k_La goes up from 69.7/h to 88.5/h as N increases from 60 to 160 rpm. However, k_La does not keep increasing with the increase of N but drops to the minimum value of 61.9/h at N=110 rpm. This is because the interphase contact area is the smallest when the gas-liquid interface is parallel to the bottom of the bioreactor at N=110 rpm. Hence, to improve OTR, it is recommended to select an appropriate revolution speed to avoid such an occurrence.

According to Barrett et al. [41], the minimum k_La which is sufficient to support the oxygen demand of 10^6 cells/mL is 1/h. In high-density culture of animal cells (>1.4×10^7 cells/mL), k_La must be at least 12/h [42]. However, for the planetary centrifugal bioreactor studied in this paper, k_La ranges from 50 to 250/h, which well satisfies the oxygen demand of cell culture. Compared with conventional bioreactors for culture of animal cells, e.g., stirred tank bioreactors whose k_La is 1-35/h at an agitation speed of 100-700 rpm [1], planetary centrifugal bioreactors have an advantage in terms of the oxygen transfer capability.

4. Mixing

Mixing is an essential function of bioreactors, which aims to eliminate the gradients of temperature, pH, dissolved oxygen concentration, by-products, etc. In the process of cell culture, effective mixing is indispensable to homogenize components distribution in fluids.

The velocity field is an important hydrodynamic parameter driving components to distribute uniformly in fluids. Fig. 10 presents the fluid velocity distributions on the horizontal and vertical cross-sections of the bioreactor. When the rotation is in the same direction as the revolution (see Fig. 10(a)) or the bioreactor involves no rotation (see Fig. 10(b)), the fluid velocity distribution on the *XZ* plane is disordered, which can be divided into three relatively isolated regions according to the fluid flow directions, namely I, II and III. Among them, the fluids in regions I and II flow away from each other, while the fluids in regions II and III flow towards each other. The fluids flow in and out at the interfaces of the three regions along the *Y*-axis direction, so efficient mixing cannot be realized on the *XZ* plane.

When the direction of rotation is opposite to that of revolution (see Fig. 10(c)), the interfaces of the three isolated regions are broken and the fluid flow directions are consistent on the *XZ* plane. When the rotation speed is further increased (see Fig. 10(d)-(f)), a large counterclockwise vortex can be observed along the boundary of the fluids and a smaller vortex is generated below the gas-liquid interface in the distal region. The large vortex constitutes a principal circulation, which is similar to the annular vortex observed by Rodriguez et al. [26] in their experiment, and the materials in this circulating flow can be rapidly mixed. The fluid velocity distribution on the *XZ* plane with respect to i shows that the rotation in the opposite direction to the revolution is conducive to the mixing effect of the planetary centrifugal bioreactor.

In spite of the changes of i, the fluid flow directions on the *XY* plane (see Fig. 10(g) and (h)) are the same as that of the bioreactor, that is, the fluids rotate around the *Z*-axis in the three-dimensional space. However, no effective principal vortex is formed on the *XY* plane. Although i does not change the fluid flow directions on the *XY* plane, it changes the fluid velocity magnitude. Whether on the *XY* plane or the *XZ* plane, the fluid velocity magnitude changes in a wider range at i=1 than at i=−1, indicating that the velocity gradient at i=1 is greater. The velocity gradient is

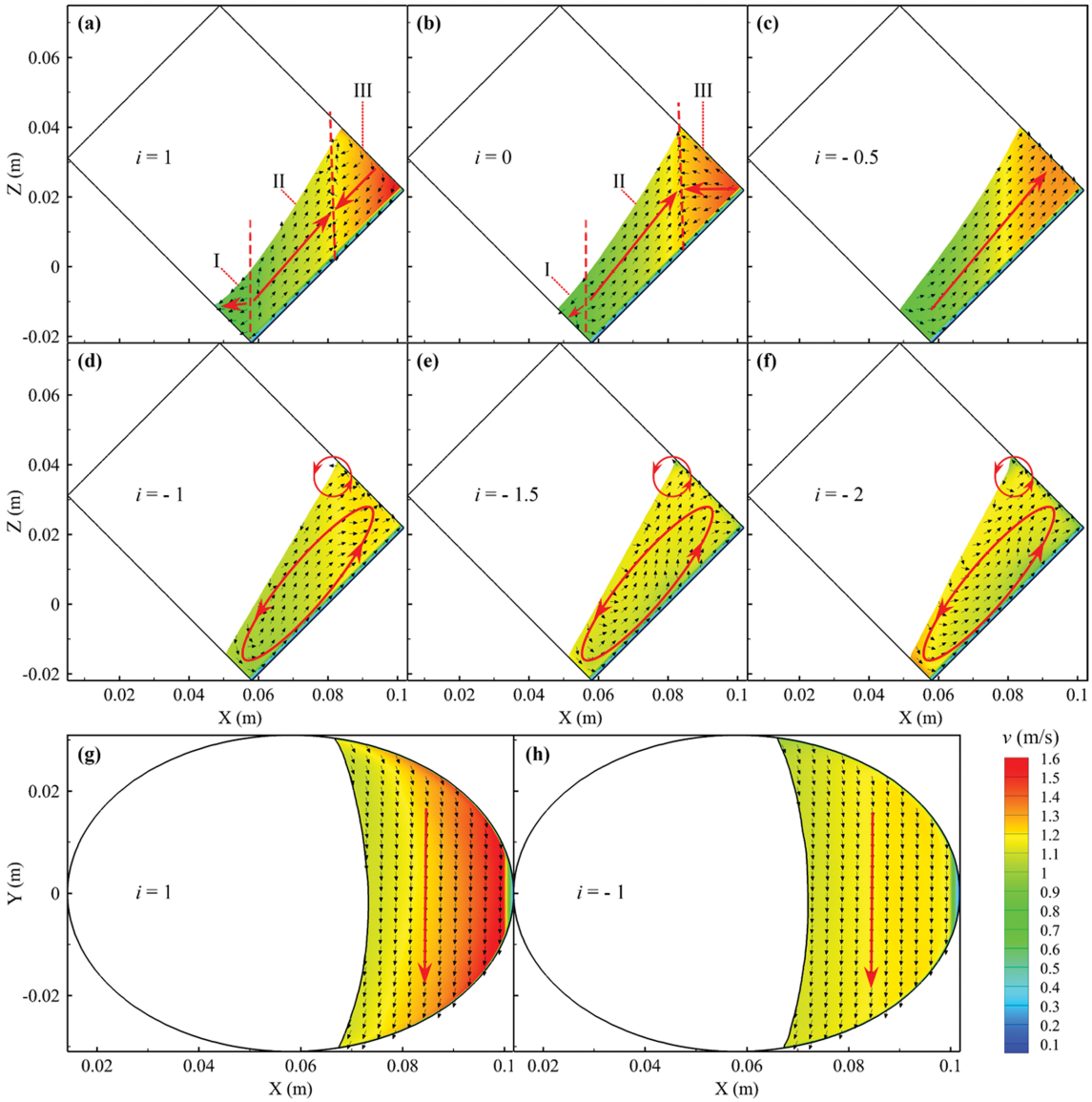

Fig. 10. Fluid velocity distribution with respect to i at N=140 rpm and β_{re}=0. (a)-(f) on the *XZ* plane with y=0; (g) and (h) on the *XY* plane with z=0.022 m. The legend at the bottom right represents the fluid velocity magnitude.

the main cause for the generation of shear stress and this is why the average and maximum shear stresses at i=1 are higher than those at i=−1 for a given N (which is discussed in detail in the next section.).

In industrial production, the fluids in bioreactors are often in the turbulent state, because the vortexes in turbulent flows can greatly improve the effect of back mixing [43]. Therefore, the turbulence intensity (I) can be used as an indicator for evaluating the mixing efficiency of bioreactors, which is calculated as follows [40]:

$$I = \frac{1}{u}\sqrt{\frac{2}{3}k} \tag{11}$$

where u represents the mean fluid velocity and k is the turbulence kinetic energy.

The turbulence intensity describes the degree of velocity fluctuation and interaction of fluid micro-masses. The greater the turbulence intensity is, the greater the momentum and mass transfer between fluid micro-masses, and the better the mixing effect. In Fig. 11, it can be seen that the rotation speed has a significant effect on the turbulence intensity. The turbulence intensity is the smallest at i=0 for a given N. As N increases from 90 to 160 rpm, the turbulence intensity at i=−1 is 9.1%, 6.9%, 21.5% and 37.1% higher than that at i=1, respectively. This indicates that turbulent mixing is promoted when the rotation is in the opposite direction to the revolution. When i<0, the turbulence intensity increases along with the increase of the rotation speed for a given N. When i is kept constant, the higher N is, the greater the turbulence intensity. This is because the energy input to the fluids is increased, resulting in an increase in the kinetic energy of fluid micro-masses. Therefore, the velocity fluctuation and the turbulence intensity increase accordingly.

The increase of energy input is a traditional solution to enhance

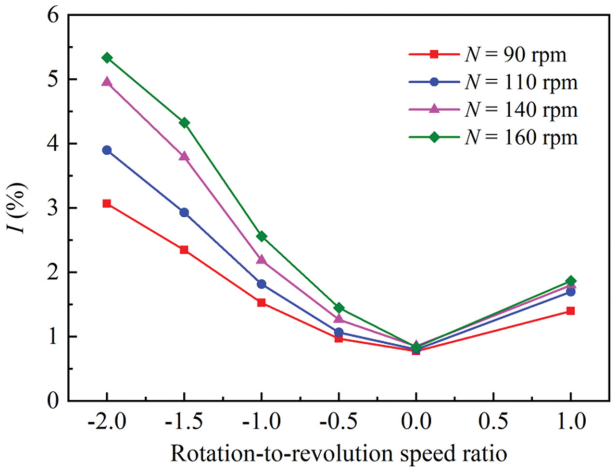

Fig. 11. Turbulence intensity of fluids under different operating conditions.

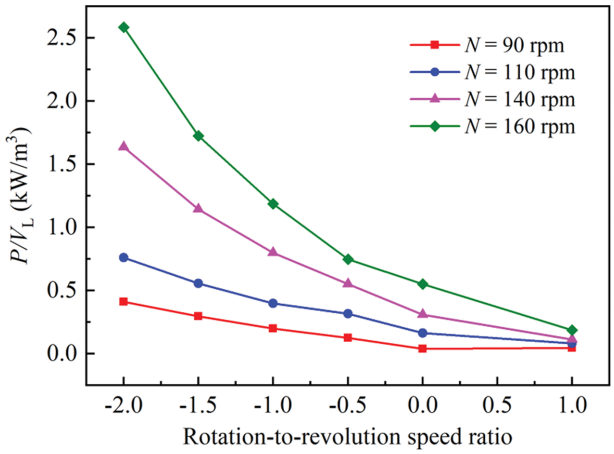

Fig. 12. Influence of revolution and rotation speeds on the volumetric power consumption.

the mixing efficiency. This is because energy is consumed during the collision and friction of fluid micro-masses and given off in form of heat. The volumetric power consumption is usually used to represent the mixing degree of fluids, which is given as follows [34]:

$$P/V_L = \frac{2\pi N M_R}{V_L} + \frac{2\pi n M_r}{V_L} \tag{12}$$

where M_R and M_r are the revolution torque and the rotation torque, respectively.

According to the existing literature, the volumetric power consumption of conventional impeller stirred bioreactors varies from 0.8 to 2.6 kW/m^3 at the rotation speed of 100-680 rpm [44]. As can be seen from Fig. 12, the volumetric power consumption of the planetary centrifugal bioreactor studied in this paper is of the same order of magnitude as that of impeller-stirred bioreactors. The volumetric power consumption decreases monotonically with the increase of i. As N increases from 90 to 160 rpm, the volumetric power consumption at i=−1 shows an improvement of 3.3%, 3.8%, 6.1% and 5.3% over that at i=1, respectively. This further proves that the rotation in the opposite direction to the revolution is advantageous, which is consistent with the findings of Chergui et al. [18].

Büchs et al. [45] reported that the fluids are more likely to be in the "out-of-phase" state as the revolution speed increases, which is manifested by a decrease in the volumetric power consumption. In this work, when i is kept constant, the volumetric power consumption always increases with the increase of N, suggesting that the fluids in the planetary centrifugal bioreactor are in the "in-phase" state all the time, namely, in normal state. Therefore, the operating conditions are reasonable.

5. Shear Environment

The shear environment is also a key factor in the design and scale-up of bioreactors, because a high shear stress will reduce the activity of cells and even cause irreversible mechanical damage to the morphology of cells, especially for some shear-sensitive cells, e.g. mammalian cells [46].

In three, the strain rate can be described by a symmetric second-order tensor consisting of nine components as follows:

$$\mathbf{E} = \begin{bmatrix} e_{xx} & e_{xy} & e_{xz} \\ e_{yx} & e_{yy} & e_{yz} \\ e_{zx} & e_{zy} & e_{zz} \end{bmatrix} \tag{13}$$

where e_{xx}, e_{yy} and e_{zz} are three normal (expansion or contraction) strain rate components. The remaining six components are tangential (shear) strain rate components, which can be calculated by the corresponding velocity gradient as follows [47]:

$$\begin{cases} e_{xy} = e_{yx} = \frac{1}{2}\left(\frac{\partial u_x}{\partial y} + \frac{\partial u_y}{\partial x}\right) \\ e_{xz} = e_{zx} = \frac{1}{2}\left(\frac{\partial u_x}{\partial z} + \frac{\partial u_z}{\partial x}\right) \\ e_{yz} = e_{zy} = \frac{1}{2}\left(\frac{\partial u_y}{\partial z} + \frac{\partial u_z}{\partial y}\right) \end{cases} \tag{14}$$

The magnitude of the strain rate tensor is calculated as follows [47]:

$$|\mathbf{E}| = \sqrt{2E_{ij}E_{ij}} = \left[2(e_{xx}^2 + e_{yy}^2 + e_{zz}^2) + 4(e_{xy}^2 + e_{xz}^2 + e_{yz}^2)\right]^{1/2} \tag{15}$$

Since this paper is focused on the damages to cells caused by the shear strain rate, the scalar measure of shear strain rate can be expressed as follows:

$$e = 2(e_{xy}^2 + e_{xz}^2 + e_{yz}^2)^{1/2} \tag{16}$$

According to Newton's law of inner friction, the scalar measure of shear stress can be calculated as follows [48]:

$$\tau = \mu e = \mu\left[\left(\frac{\partial u_x}{\partial y} + \frac{\partial u_y}{\partial x}\right)^2 + \left(\frac{\partial u_x}{\partial z} + \frac{\partial u_z}{\partial x}\right)^2 + \left(\frac{\partial u_y}{\partial z} + \frac{\partial u_z}{\partial y}\right)^2\right]^{1/2} \tag{17}$$

In the planetary centrifugal bioreactor, the shear stress is mostly less than 0.16 Pa, as shown in Fig. 13. The maximum shear stress occurs near the wall of the bioreactor due to the adhesion of the wall. The viscosity of the gas phase is negligible, so a very low shear stress can be observed at the gas-liquid interface.

Fig. 14 shows the distribution of shear stress at N=140 rpm

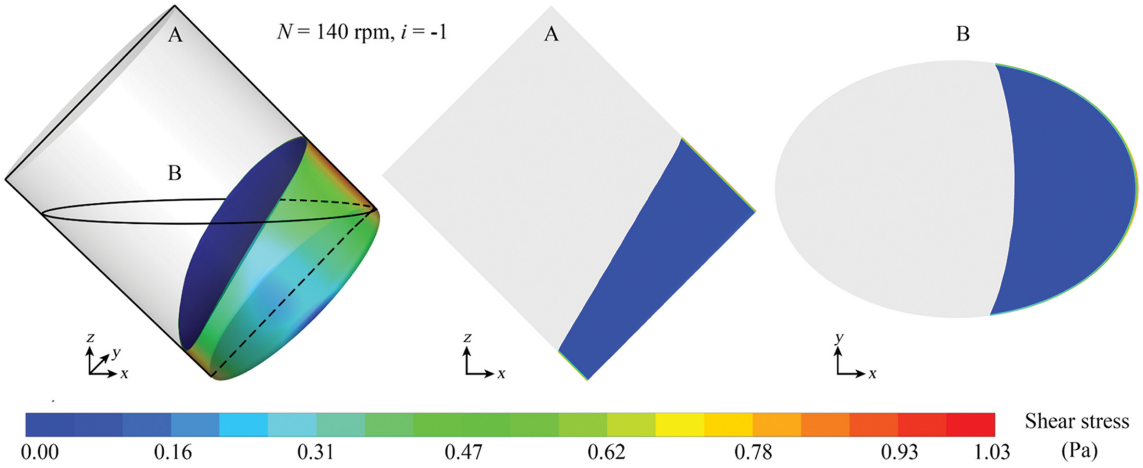

Fig. 13. Shear stress distribution of the liquid phase in the planetary centrifugal bioreactor.

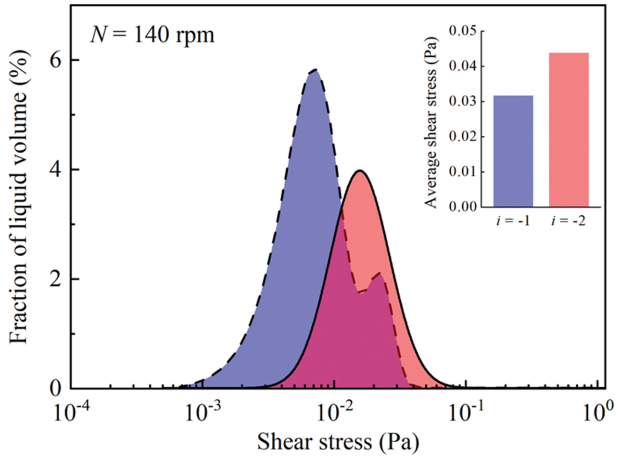

Fig. 14. Comparison of shear stress distributions in the planetary centrifugal bioreactor at i=−1 and i=−2.

with different rotation-to-revolution speed ratios. The simulation results show that the shear stress is below 0.4 Pa in more than 96.4% of the vessel zone. The stress concentration interval at i=−2 is greater than that at i=−1, resulting in a greater average shear stress of 0.044 Pa.

To evaluate the effects of the operating conditions on the shear environment, the average and maximum shear stresses in the planetary centrifugal bioreactor are computed with respect to N and i. As shown in Fig. 15, the average and maximum shear stresses rise along with the increase of N for a given i. In addition, the rotation in the same direction as the revolution generates a higher shear stress than the rotation in the opposite direction to the revolution under the same conditions. This is because the average and maximum shear stresses at i=−1 are at least 3.4% and 28.3% lower than those at i=1, respectively, as N varies from 90 to 160 rpm.

The effect of shear stress on the cell growth has been widely reported. The shear stress in conventional bioreactors, e.g., stirred tank bioreactors, is 1.97-3.96 Pa at the revolution speed of 75-150 rpm, which is tolerable for large microalgae cells [3]. The death rate of *Carthamus tinctorius* L. cells begins to increase when the average shear stress exceeds 0.55 Pa and the maximum shear stress is greater than 4.00 Pa [29,49]. In this work, the planetary centrifugal bioreactor shows an average shear stress of 0.01-0.05 Pa and the maximum shear stress ranges from 0.6 to 1.7 Pa. Therefore, the

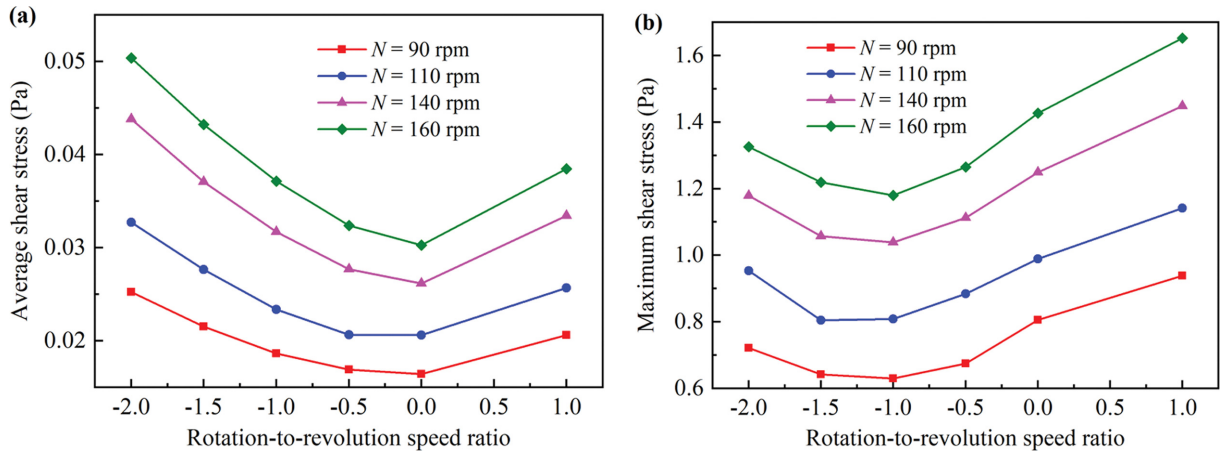

Fig. 15. Effect of different operating conditions on the average shear stress (a) and the maximum shear stress (b).

planetary centrifugal bioreactor can provide a suitable shear environment for the growth of shear-sensitive cells.

CONCLUSIONS

We have shown the potential of planetary centrifugal bioreactors for cell culture. A validated CFD model was used to study the effect of operating conditions on the oxygen transfer rate, mixing characteristics and shear environment of a planetary centrifugal bioreactor. The results show that the volumetric mass transfer coefficient (k_La) is above 50/h and the shear stress is mostly below 0.4 Pa, which can meet the needs of culturing oxygen-consuming and shear-sensitive cells. The results also show that k_La, the mixing efficiency and the shear stress increase along with the increase of the revolution and rotation speeds. With the revolution speed of 140 rpm, k_La, the turbulence intensity and the volumetric power consumption at i=−1 are 3.4%, 21.5% and 6.1% higher than those at i=1, while the average and maximum shear stresses decrease by 5.2% and 28.3%, respectively. Therefore, the rotation in the opposite direction to the revolution is beneficial to the performance of the bioreactor. The maximum rotation speed in the opposite direction to the revolution contributes to the occurrence of front waves and a large circulating flow is generated in the axial direction of the bioreactor, which helps to enhance the mass transfer and mixing of the liquid phase. When the gas-liquid interface is parallel to the bottom of the bioreactor, the oxygen transfer rate is reduced, because the gas-liquid interface area is the smallest in this case. This paper will provide a reference in designing a suitable planetary centrifugal bioreactor and determining the optimal operating conditions for culturing the selected cells.

ACKNOWLEDGEMENT

This study is supported by the National Natural Science Foundation of China (Grant Nos. 51975226 and 51605179).

NOMENCLATURE

A : gas-liquid interface area [m^2]
a : specific mass transfer area [m^2/m^3]
d : characteristic length [m]
D_L : diffusion coefficient of oxygen [m^2/s]
e : scalar measure of shear strain rate [s^{-1}]
E : strain rate tensor [s^{-1}]
E_{ij} : element of the strain rate tensor [s^{-1}]
G_b : turbulence generation due to buoyancy [$kg/m{\cdot}s^3$]
G_k : turbulence generation due to the mean velocity gradients [$kg/m{\cdot}s^3$]
H : vessel height [mm]
I : turbulence intensity [%]
i : ratio of rotation to revolution speed
k : turbulence kinetic energy [m^2/s^2]
k_L : mass transfer coefficient [m/h]
k_La : volumetric mass transfer coefficient [1/h]
M_R : revolution torque [Pa·s]
M_r : rotation torque [Pa·s]
N : revolution speed [rpm]
N_{re} : number of full revolutions
p : mean pressure [Pa[
P/V_L : volumetric power consumption [kW/m^3]
R : revolution radius [mm]
R_ε : additional term due to interaction between turbulence dissipation and mean shear in ε-transport equation of RNG k-ε
Re : Reynolds numbers
r : vessel radius [mm]
S_k : source term for k-transport equation
$S_{M,i}$: source term for momentum equation in i direction
S_ε : source term for ε-transport equation
S_φ : source term
t : time [s]
u : mean fluid velocity [m/s]
u_{ch} : characteristic velocity [m/s]
U : mean velocity vector [m/s]
$\mathbf{U}_G$: velocity vector of the gas phase [m/s]
U_i : mean velocity in i direction [m/s]
V_L : filling volume [mL]
Y_M : dilatation dissipation [$kg/m{\cdot}s^3$]

Greek Symbols

α : inclination angle [°]
α_k : inverse effective Prandtl number for turbulence kinetic energy
α_ε : inverse effective Prandtl number for turbulence kinetic energy dissipation rate
β : gyration angle [°]
β_{re} : phase angle relative to the *X*-axis [°]
γ : volume fraction of the gas phase
Γ_φ : diffusivity
ε : turbulence dissipation rate [m^2/s^3]
μ : fluid viscosity [Pa·s]
μ_t : turbulent viscosity or eddy viscosity [Pa·s]
ρ : density [kg/m^3]
τ : scalar measure of shear stress [Pa]
ϕ : universal variable
Ω : angular velocity of revolution [rad/s]
ω : angular velocity of rotation [rad/s]
ω_x : angular velocity component along the *X*-axis
ω_y : angular velocity component along the *Y*-axis
ω_z : angular velocity component along the *Z*-axis

Abbreviations

CFD : Computational Fluid Dynamics
MRF : multiple reference frame
OTR : oxygen transfer rate
PISO : pressure-implicit with splitting of operators
PRESTO! : pressure staggering option
RANS : Reynolds-averaged Navier-Stokes
SM : sliding mesh
VOF : volume of fluid

REFERENCES

1. M. M. Buffo, L. J. Corrêa, M. N. Esperança, A. J. G. Cruz, C. S. Fari-

nas and A. C. Badino, *Biochem. Eng. J.*, **114**, 130 (2016).
2. S. Smetana, M. Sandmann, S. Rohn, D. Pleissner and V. Heinz, *Bioresour. Technol.*, **245**, 162 (2017).
3. R. Verma, L. Mehan, R. Kumar, A. Kumar and A. Srivastava, *Biochem. Eng. J.*, **151**, 107312 (2019).
4. H. Hang, Y. Guo, J. Liu, L. Bai, J. Xia, M. Guo and M. Hui, *Biotechnol. Bioproc. E.*, **16**, 567 (2011).
5. M. J. De Jesus, P. Girard, M. Bourgeois, G. Baumgartner, B. Jacko, H. Amstutz and F. M. Wurm, *Biochem. Eng. J.*, **17**, 217 (2004).
6. S. O. Enfors, M. Jahic, A. Rozkov, B. Xu, M. Hecker, B. Jürgen, E. Krüger, T. Schweder, G. Hamer, D. O'Beirne, N. Noisommit-Rizzi, M. Reuss, L. Boone, C. Hewitt, C. McFarlane, A. Nienow, T. Kovacs, C. Trägårdh, L. Fuchs, J. Revstedt, P. C. Friberg, B. Hjertager, G. Blomsten, H. Skogman, S. Hjort, F. Hoeks, H. Y. Lin, P. Neubauer, R. van der Lans, K. Luyben, P. Vrabel and Å. Manelius, *J. Biotechnol.*, **85**, 175 (2001).
7. T. Tanzeglock, M. Soos, G. Stephanopoulos and M. Morbidelli, *Biotechnol. Bioeng.*, **104**, 360 (2009).
8. C. Zupke, A. J. Sinskey and G. Stephanopoulos, *Appl. Microbiol. Biot.*, **44**, 27 (1995).
9. J. Zhong, *Korean J. Chem. Eng.*, **27**, 1035 (2010).
10. T. T. Devi and B. Kumar, *Korean J. Chem. Eng.*, **31**, 1339 (2014).
11. A. Pan, M. Xie, J. Xia, J. Chu and Y. Zhuang, *Korean J. Chem. Eng.*, **35**, 61 (2018).
12. P. Riegler, T. Chrusciel, A. Mayer, K. Doll and D. Weuster-Botz, *Biochem. Eng. J.*, **141**, 89 (2019).
13. J. Xia, Y. Wang, S. Zhang, N. Chen, P. Yin, Y. Zhuang and J. Chu, *Biochem. Eng. J.*, **43**, 252 (2009).
14. Y. Liu, J. Chen, J. Song, Z. Hai, X. Lu, X. Ji and C. Wang, *Bioresour. Technol.*, **272**, 360 (2019).
15. A. C. Badino, M. C. R. Facciotti and W. Schmidell, *Biochem. Eng. J.*, **8**, 111 (2001).
16. Z. J. Li, V. Shukla, K. Wenger, A. Fordyce, A. G. Pedersen and M. Marten, *Biotechnol. Bioeng.*, **77**, 601 (2002).
17. F. Garcia-Ochoa and E. Gomez, *Biotechnol. Adv.*, **27**, 153 (2009).
18. N. Chergui, M. Lateb, É. Lacroix and L. Dufresne, *Chem. Eng. Res. Des.*, **102**, 100 (2015).
19. U. Massing, S. Cicko and V. Ziroli, *J. Control. Release*, **125**, 16 (2008).
20. Y. Yamaga, M. Kanatani and S. Nomura, *J. Prosthodontic Res.*, **59**, 71 (2015).
21. M. A. Raza, A. V. K. Westwood and C. Stirling, *Mater. Chem. Phys.*, **132**, 63 (2012).
22. J. Bridgwater, *Particuology*, **10**, 397 (2012).
23. K. J. Son, *Korea-Aust. Rheol. J.*, **30**, 199 (2018).
24. W. Weheliye, M. Yianneskis and A. Ducci, *AIChE J.*, **59**, 334 (2013).
25. A. Ducci and W. H. Weheliye, *AIChE J.*, **60**, 3951 (2014).
26. G. Rodriguez, M. Micheletti and A. Ducci, *Chem. Eng. Res. Des.*, **132**, 890 (2018).
27. Z. Lu, K. Wang, G. Jin, K. Huang and J. Huang, *J. Chem. Technol. Biotechnol.*, **93**, 810 (2017).
28. M. Discacciati, D. Hacker, A. Quarteroni, S. Quinodoz, S. Tissot and F. M. Wurm, *Int. J. Numer. Meth. Fl.*, **71**, 294 (2013).
29. Y. Liu, Z. Wang, J. Zhang, J. Xia, J. Chu, S. Zhang and Y. Zhuang, *Biochem. Eng. J.*, **113**, 66 (2016).
30. L. Zhu, B. Song, Z. Wang, D. T. Monteil, X. Shen, D. L. Hacker, M. De Jesus and F. M. Wurm, *Biotechnol. Progr.*, **33**, 192 (2017).
31. M. Mansour, P. Khot, P. Kováts, D. Thévenin, K. Zähringer and G. Janiga, *Chem. Eng. J.*, **383**, 123121 (2020).
32. E. Bumrungthaichaichan, *Korean J. Chem. Eng.*, **33**, 3050 (2016).
33. Y. He, A. E. Bayly, A. Hassanpour, M. Fairweather and F. Muller, *Chem. Eng. Sci.*, **212**, 115333 (2020).
34. A. Kazemzadeh, C. Elias, M. Tamer, A. Lohi and F. Ein-Mozaffari, *Chem. Eng. Sci.*, **219**, 115606 (2020).
35. F. Auger, G. Delaplace, L. Bouvier, A. Redl, C. André and M. Morel, *J. Food Eng.*, **118**, 350 (2013).
36. I. A. Escamilla-Ruíz, F. Z. Sierra-Espinosa, J. C. García, A. Valera-Medina and F. Carrillo, *Heat Mass Transfer.*, **53**, 2933 (2017).
37. E. Bumrungthaichaichan and S. Wattananusorn, *J. Chin. Inst. Eng.*, **42**, 428 (2019).
38. J. Büchs, U. Maier, S. Lotter and C. P. Peter, *Biochem. Eng. J.*, **34**, 200 (2007).
39. P. Ducommun, P. Ruffieux, M. Furter, I. Marison and U. von Stockar, *J. Biotechnol.*, **78**, 139 (2000).
40. C. Li, J. Xia, J. Chu, Y. Wang, Y. Zhuang and S. Zhang, *Biochem. Eng. J.*, **70**, 140 (2013).
41. T. A. Barrett, A. Wu, H. Zhang, M. S. Levy and G. J. Lye, *Biotechnol. Bioeng.*, **105**, 260 (2010).
42. P. Ruffieux, U. von Stockar and I. W. Marison, *J. Biotechnol.*, **63**, 85 (1998).
43. S. C. Kaiser, M. Kraume and D. Eibl, *Chem. Ing. Tech.*, **88**, 77 (2016).
44. M. Xie, J. Xia, Z. Zhou, G. Zhou, J. Chu, Y. Zhuang, S. Zhang and H. Noorman, *Chem. Eng. Sci.*, **106**, 144 (2014).
45. J. Büchs, U. Maier, C. Milbradt and B. Zoels, *Biotechnol. Bioeng.*, **68**, 594 (2000).
46. M. A. Garcia-Briones and J. J. Chalmers, *Biotechnol. Bioeng.*, **44**, 1089 (1994).
47. ANSYS, *ANSYS Fluent Theory Guide*, release 19.0 (2017).
48. L. Zhu, B. Song and Z. Wang, *J. Chem. Technol. Biotechnol.*, **94**, 2212 (2019).
49. Y. Liu, Z. Wang, J. Xia, C. Haringa, Y. Liu, J. Chu, Y. Zhuang and S. Zhang, *Biochem. Eng. J.*, **114**, 209 (2016).